

Predicting biofilm deformation with a viscoelastic phase field model: modeling and experimental studies

Mengfei Li¹, Karel Matouš¹, and Robert Nerenberg¹

¹University of Notre Dame

April 28, 2020

Abstract

Biofilms commonly develop in flowing aqueous environments, where the flow causes the biofilm to deform. Because biofilm deformation affects the flow regime, and because biofilms behave as complex heterogeneous viscoelastic materials, few models are able to predict biofilm deformation. In this study, a phase field continuum model coupled with the Oldroyd-B constitutive equation was developed and used to simulate biofilm deformation. The accuracy of the model was evaluated using two types of biofilms: a synthetic biofilm, made from alginate mixed with bacterial cells, and a *Pseudomonas aeruginosa* biofilm. Shear rheometry was used to experimentally determine the mechanical parameters for each biofilm, as inputs for the model. Biofilm deformation under fluid flow was monitored experimentally using optical coherence tomography. The fit between the experimental and modeling geometries after fluid-driven deformation was very good, with relative errors of 12.8% for synthetic biofilm and 22.2% for homogenized *P. aeruginosa* biofilm. This is the first demonstration of the effectiveness of a viscoelastic phase field biofilm model. This model provides an important tool for predicting biofilm viscoelastic deformation. It also can benefit the design and control of biofilms in engineering systems.

1. Introduction

Biofilms are complex aggregates of microorganisms embedded in a matrix of extracellular polymeric substances (EPS) (Flemming & Wingender, 2010; Hall-Stoodley et al., 2004). Biofilms are ubiquitous in the natural environment, and have profound impacts on engineering systems and human health (Chen et al., 2014; Hall-Stoodley et al., 2004). For example, biofilm detachment in the food industry and drinking water systems may cause pathogen-related diseases (Shaheen et al., 2019; Shen et al., 2015; Wéry et al., 2008). The EPS matrix, which is a major component of biofilms, protects bacteria from unfavorable environments and chemical stresses (Desmond et al., 2018; Flemming & Wingender, 2010; Simões et al., 2009; Sutherland, 2001), and provides mechanical stability.

Most biofilms develop in flowing aqueous environments, where the flow provides a mechanical loading on the biofilm. The hydrodynamic conditions may result in biofilm deformation, erosive detachment (small particle loss from the biofilm exterior), or sloughing (major biofilm loss) (Blauert et al., 2015; Jafari et al., 2018; Paul et al., 2012; J. B. Xavier et al., 2005). On the other hand, the biofilm's physical response to mechanical forces, such as deformation and detachment, may affect their structure, composition, porosity, mass transfer characteristics, and fluid dynamic forces (Laspidou & Rittmann, 2004; Purevdorj et al., 2002; Stoodley et al., 2002, 1999). The interactions of hydrodynamics and biofilms are affected by the biofilm's mechanical properties. Thus, in order to control biofilms effectively, it is critical to understand biofilm mechanical properties and their impact on stress-induced deformation and detachment.

Biofilms behave as viscoelastic materials (Jones et al., 2011; Klapper et al., 2002; Towler et al., 2003), which allows them to adapt and form versatile structures under fluid flow (Hall-Stoodley et al., 2004). This also affects their detachment. However, biofilms are complex, both in microbial ecology, morphology, and EPS

chemical composition. This provides them with a great spatial variability (i.e., heterogeneity) of mechanical properties, as well as a potentially large differences between mechanical properties among different biofilms (Böl et al., 2012; Galy et al., 2012; Pavissich et al., 2020; Shaw et al., 2004). This is further complicated by the large variety of experimental techniques used to measure mechanical properties, and the different types of parameters obtained. This makes it difficult to compare the results of different studies (Böl et al., 2012; Gloag et al., 2019; Tallawi et al., 2017). Additionally, while an increasing body of researchers is reporting on biofilm mechanical properties, it is not clear how to use them to predict biofilm deformation and detachment. Having well characterized mechanics and suitable models could allow more effective control of engineered, medical, and other biofilms.

In recent years, researchers have developed mathematical models that incorporate biofilm mechanical behavior, allowing the prediction of biofilm deformation (e.g., Ehret & Böl, 2013; Laspidou et al., 2005; Picioreanu et al., 2018, 2001; Stewart, 1993). Several previous studies (e.g., Picioreanu et al., 2001; Radu et al., 2010; Stewart, 1993; Xavier et al., 2005) focused on the biofilm development considering shear-induced detachment via cohesive strength, or with empirical detachment rate. These models treated biofilms as rigid bodies without deformation (Klapper & Dockery, 2010).

Detachment is a natural process controlled by the biofilm's mechanical properties (i.e., cohesive strength). However, in cases where biofilm deformation is of interest, it is more accurate to include the effects of deformation on the fluid flow regime, as with fluid-structure interaction models. In order to achieve this, many researchers have simplified biofilms as purely elastic solids, since the short-term response of biofilms is mostly elastic (Dupin et al., 2001; Picioreanu et al., 2018; Taherzadeh et al., 2010). However, viscous behavior may be significant when the time scales are similar to biofilm relaxation (Alpkvist & Klapper, 2007; Liou et al., 2019). For example, Towler et al. (2007) developed a numerical model based on Burger's material law to describe the biofilm viscoelastic behavior under fluid flows. Alpkvist and Klapper (2007) applied the particle-based immersed boundary method to demonstrate biofilm deformation and detachment under fluid flows. Traditional fluid-structure interaction models can capture the physical behavior accurately, with certain limitations.

Unfortunately, the direct coupling of the fluid domain to the solid domain creates significant computational difficulties, especially for tracking the interface (Mokbel et al., 2018; Rubenstein et al., 2015). Configuration changes, such as large deformations or particle breakup, are difficult to capture with these models. Thus, alternative models are necessary to overcome these limitations.

Multi-phase models have been applied to biofilm studies by treating biofilms as fluids (Alpkvist et al., 2006; Tierra et al., 2015; Zhang et al., 2008b). In particular, phase field (PF) models have been proposed to predict biofilm deformation and detachment (Tierra et al., 2015; Zhang et al., 2008a, 2008b; Zhao et al., 2016). In PF models, the phase-field variable, based on the free energy of the system, controls the morphological changes of the interface without the consideration of boundary tracking (Gao et al., 2009; Zheng & Karniadakis, 2016). Besides, using the Eulerian PF models avoids mesh limitations for large deformations (Gao et al., 2009; Zheng & Karniadakis, 2016). Also, by assuming the biofilm is a viscous or viscoelastic fluid, biofilm detachment due to mechanical stresses can be achieved.

While PF models have the potential to accurately simulate biofilm large deformation and detachment, there are few validation studies. Even with the experimental studies of PF models being reported in other fields (Bai et al., 2017; Han et al., 2015; Nguyen et al., 2016; Pham et al., 2017; Wen et al., 2000), the experimental validation of a PF biofilm model is lacking.

In our study, we determined biofilm mechanical properties experimentally, input them into a continuum PF model, and showed the model can accurately predict biofilm deformation under fluid flow. For this purpose, the Oldroyd-B constitutive equation was used to model biofilm viscoelastic behavior. A synthetic biofilm made of microbial cells embedded in alginate was initially used for model validation, as it is more homogeneous. Further studies were then carried out on a *Pseudomonas aeruginosa* biofilm. This study opens the use of PF continuum modeling for a wide range of biofilm applications.

2. Materials and Methods

2.1 The phase field model

The PF model for two-phase flow was applied to simulate biofilm deformation under fluid flow. This two-dimensional continuum biofilm model was implemented using COMSOL Multiphysics (COMSOL v5.4, Comsol Inc, Burlington, MA) with finite element method. COMSOL has computational fluid dynamics and phase field modeling as built-in features, and we implemented the constitutive equation (i.e., Oldroyd-B viscoelastic model) for the biofilm viscoelastic behavior using partial differential equation (PDE) module. The biofilm was considered an incompressible viscoelastic liquid.

2.1.1 Phase field model

The phase-field model was adapted from Yue et al. (2006) and Zhang et al. (2010), and applied to biofilm-fluid interactions. Two types of incompressible, immiscible fluids were studied as two components of a single fluid. The fluid interface was assumed to be a thin, nonzero thickness transition region with distributed interfacial forces (Kim, 2012).

In our model, we consider the bulk water phase (solvent) and biofilm as two immiscible fluids. The PF variable $\phi \in [-1, 1]$ is defined as the difference between volume fractions of each component. $V_b + V_s = 1$, $V_b = \frac{1+\phi}{2}$, $V_s = \frac{1-\phi}{2}$, $\rho(\phi) = V_b\rho_b + V_s\rho_s$, where V_b and V_s are the volume fractions of biofilm and solvent. ρ is the density of fluids [kg/m³], ρ_b represents the density of a biofilm and ρ_s represents the density of a solvent. The governing equation for the PF model is the advective Cahn-Hilliard equation, which uses a chemical potential representing the diffuse interface of two fluids:

$$\frac{\partial \phi}{\partial t} + \mathbf{u} \cdot \nabla \phi = \nabla \cdot \frac{\gamma \varphi}{\varepsilon^2} \nabla \psi, \quad \psi = -\nabla \cdot \varepsilon^2 \nabla \phi + (\phi^2 - 1) \phi,$$

where \mathbf{u} is the fluid velocity [m/s], γ is the mobility [m³[?]/s/kg], φ is the mixing energy density [N], and ε is the interface thickness parameter [m]. Another dependent variable of the PF model is phase field variable ψ . The mixing energy density is defined as: $\phi = \frac{3\vartheta\varepsilon}{\sqrt{8}}$, where ϑ is surface tension coefficient [N/m]. The mobility γ is defined as: $\gamma = \chi\varepsilon^2$, where χ is the mobility coefficient [m[?]/s/kg].

2.1.2 Navier-Stokes equation

The incompressible Navier-Stokes equations were applied to describe the transport of momentum and mass of both solvent liquid and biofilm liquid:

$$\rho \frac{\partial \mathbf{u}}{\partial t} + \rho(\mathbf{u} \cdot \nabla) \mathbf{u} = \nabla \cdot \boldsymbol{\sigma} + \frac{\varphi}{\varepsilon^2} \psi \cdot \nabla \phi, \quad \boldsymbol{\sigma} = -p\mathbf{1} + \mathbf{T}(\phi), \quad \nabla \cdot \mathbf{u} = 0,$$

where $\boldsymbol{\sigma}$ is the Cauchy stress tensor, \mathbf{T} is the deviatoric part of the stress tensor, p is the pressure [Pa], and $\mathbf{1}$ is the second-order identity tensor.

2.1.3 Constitutive equation of viscoelasticity

To study the viscoelastic fluids, we applied the Oldroyd-B model by considering the water as a Newtonian fluid and the biofilm as a non-Newtonian fluid. The constitutive Oldroyd-B equation is given by

$$\boldsymbol{\tau} + \lambda \tau^\nabla = 2\mu_b \mathbf{d}, \quad \tau^\nabla = \frac{\partial \boldsymbol{\tau}}{\partial t} + \mathbf{u} \cdot \nabla \boldsymbol{\tau} - (\nabla \mathbf{u})^T \cdot \boldsymbol{\tau} - \boldsymbol{\tau} \cdot (\nabla \mathbf{u}),$$

$$\mathbf{T}(\phi) = V_b(\boldsymbol{\tau} + 2\mu_s \mathbf{d}) + V_s(2\mu_s \mathbf{d}),$$

where $\boldsymbol{\tau}$ is the extra (i.e., viscous) stress tensor, τ^∇ denotes the upper-convected time derivative (Oldroyd derivative) of the stress tensor, $\lambda = \mu_b/G_b$ is the biofilm elastic relaxation time [s]. G_b is the biofilm shear modulus [Pa]. μ_b and μ_s are dynamic viscosities of the biofilm and solvent [Pa[?]/s], respectively. Here we define $\boldsymbol{\sigma}_e = 2\mu_s \mathbf{d}$ as the elastic deviatoric component of the stress tensor. Finally, \mathbf{d} is the symmetric part of the velocity gradient, $\mathbf{d} = \frac{1}{2}(\nabla \mathbf{u} + (\nabla \mathbf{u})^T)$.

2.1.4 Boundary and initial conditions

Fig. 1 shows the coordinate system for the 2-dimensional (2D) domain. For boundary conditions, we applied constant parabolic velocity to the upstream flow and set zero pressure at the downstream. Considering the 2D domain, for velocity vector $\mathbf{u} = \{u_1, u_2\}^T$ upstream, we set: $u_1 = u_0$, $u_2 = 0$. Along the wall, we consider $\mathbf{u} = \mathbf{0}$ and $\tau_{yy} = 0$. The gradient of x-velocity and xx component of extra stress is 0. Thus, the boundary conditions for stress τ would be as following:

$$\tau_{xx} = 2\mu_b\lambda\left(\frac{\partial u}{\partial y}\right)^2, \tau_{xy} = \mu_b\frac{\partial u}{\partial y}, \tau_{yy} = 0,$$

where $\tau =$

]. [The initial condition for the velocity and extra stress were set as $\mathbf{u} = \mathbf{0}$ and $\tau = \mathbf{0}$ in the whole domain.

2.1.5 Numerical implementation

The average bulk flow velocity was ramped up at the beginning of the simulation (within 1 s) to reduce the computational difficulties. The mechanical parameters of the biofilm were obtained from rheometer tests (see Section 2.3), including the viscosity and shear modulus. All parameters are listed in Table 1. To accommodate the incompressibility, we used traditional Lagrange mixed finite elements (Hughes, 2012). In particular, we used the quadratic triangular elements for the velocity and extra stress components, and the linear elements for the pressure discretization. To alleviate the numerical difficulty caused by the Oldroyd-B equation, we implemented the Galerkin/Least squares stabilization (Craven, Rees, & Zimmerman, 2006; Rajagopal & Das, 2016). We also performed model verification and mesh convergence tests to ensure that the results were not affected by the mesh size (see Supplementary Information SI). Based on the results, a maximum mesh size of 50 μm was chosen for this study.

2.2 Preparation of synthetic biofilm and growth of *Pseudomonas aeruginosa* biofilm

Synthetic biofilms were prepared from alginate (Acros Organics, USA) with internal release of calcium ions using D-glucono- δ -lactone (GDL) and calcium carbonate. As a slowly hydrolyzing lactone, GDL can control the pH and slow the release of Ca^{2+} ions, which crosslink the alginate gel internally (Pawar & Edgar, 2012). This results in more homogeneous mechanical properties. The method was modified from Draget et al. (1991). Bacterial cells were grown from using sludge from the local South Bend Wastewater Treatment Plant, South Bend, Indiana, USA (See SI). The mixture of alginate/ Ca^{2+} /bacteria was naturally dried at room temperature for 24 h to achieve full gelation. After full gelation, the alginate sample was tested immediately in the rheometer or with deformation experiments. The detailed information of synthetic biofilm preparation is provided in the SI.

P. aeruginosa PAO1 (ATCC 15692) labeled with green fluorescent protein (GFP) was used for the biofilm experiments. The growth medium (see SI) contained 100 mg/L of acetate as an electron donor and 15 $\mu\text{g}/\text{mL}$ of gentamicin sulfate (Sigma-Aldrich, USA) to maintain axenic conditions. The *P. aeruginosa* biofilm was grown in a membrane-aerated biofilm reactor (MABR), following Aybar et al. (2019). The biofilm was collected from the membrane after two weeks of growth, at which time it was approximately 800 μm thick. Approximately 2 g (wet) of biofilm was collected. The sample was mixed and homogenized by gently stirring with spatula, and tested immediately with rheometry and deformation experiments.

2.3 Rheometry analysis

In order to determine the viscoelastic parameters for the alginate and *P. aeruginosa* biofilms, a shear rheometer (Discovery HR-2 Hybrid, TA Instruments, Illinois, USA) was used. Two-step tests were performed in this study: (1) strain sweep tests were used to determine the range of linear viscoelastic behavior; (2) stress relaxation tests were carried out to obtain the mechanical properties of both biofilms. The methods were adapted from Towler et al. (2003). We first performed dynamic strain sweep tests. The dynamic strain sweep provides the information of storage (G') and loss (G'') moduli as a function of strain. Second, a strain value was chosen for stress relaxation tests within the range of linear viscoelastic behavior. The stress relaxation tests can be fitted with mathematical models and mechanical properties of biofilms can be obtained. Several mathematical models can be used to analyze the viscoelastic phenomena (Areias & Matouš, 2008), such as

Maxwell model, Kelvin-Voigt model, and four-element Burgers model. An Oldroyd-B model is an extension of the upper convected Maxwell model. Therefore, we chose the Maxwell model as the mathematical model for fitting the rheometer data. Fitted data of shear modulus (G_b) and dynamic viscosity (μ_b) were obtained, then applied to the computational model (see Sec. 2.1.3). All the rheometry analyses were performed with MATLAB (Mathworks, Natick, Massachusetts, USA, www.mathworks.com) using nonlinear least-squares solver. A detailed description of rheometer analysis and mathematical model fitting is provided in the SI.

2.4 Biofilm deformation experiments

The synthetic biofilm or homogenized *P. aeruginosa* biofilm was inserted into a cylindrical support with a dimension of 1mm \times 3mm (diameter \times height) (Fig. 2). The biofilm cylinder-shaped support was glued inside a flow cell with a dimension of 25 cm \times 10 mm \times 10 mm (length \times width \times height). The flow was driven by gravity, and the flow rate was controlled with a valve on the influent line. The large size of the water reservoir and the short duration of the experiment led to minimal changes in water level in the water reservoir, therefore providing near-constant velocities. The flow rate (u_1) was measured by directing the effluent to a graduated cylinder. Biofilm morphologies were monitored and recorded using optical coherence tomography (OCT) (Ganymede II, Thorlabs GmbH, Lübeck, Germany). The image collection software was ThorImage OCT, Version 5.0.1. The cross-sectional images of biofilm were captured by recording a real-time video of the OCT output (SI V1-V2).

2.5 Imaging processing and analysis

Imaging post-processing was performed using FIJI (Schindelin et al., 2012), Inkscape 0.91 (<https://inkscape.org>), and MATLAB Image Processing Toolbox (Mathworks, Natick, Massachusetts, USA, www.mathworks.com). Simplified biofilm geometries were created and input into the model (see SI). The displacements of biofilms in both experiments and modeling were obtained using digital image correlation (DIC) (see SI). The DIC code was modified from Eberl et al. (2006). The relative error between the experimental and modeling results was calculated as $\frac{\Sigma(|D_m - D_e|)}{\Sigma(D_e)} \times 100\%$ by a summation of every second data for the three tracking lines (shown in Fig. 7 and 9), where D_m is the displacement in the model and D_e is the displacement in the experiment.

3. Results and Discussion

3.1 Mechanical properties of synthetic and *P. aeruginosa* biofilms

Rheometry is commonly used to measure the mechanical properties of viscoelastic materials. It is also widely used to measure biofilm mechanical properties, as it is suitable for viscoelastic solids and non-Newtonian fluids. Averaged properties of a sample are measured, providing the relationship between force, deformation, and time. Our goal was to obtain the biofilm mechanical parameters as inputs for the computational model. As a first step, alginate with embedded microbial cells was used as a synthetic biofilm, since it is mechanically more homogenous and it can be formed into a regular geometry. A regular geometry is desirable for both rheometry analysis and for simulations. We also tested a homogenized *P. aeruginosa* biofilm.

In order to confirm the homogeneity of synthetic biofilms, G' and G'' from strain sweep test were discussed (Fig. 3). The storage modulus G' , representing elasticity, and loss modulus G'' , representing viscosity, were calculated. Averaged G' and G'' from synthetic biofilm were 251.3 Pa \pm 7.1 Pa and 18.2 Pa \pm 5.5 Pa, respectively. A higher G' compared to G'' also revealed that the synthetic biofilm samples were more elastic than viscous. Error bars in Fig. 3 show the standard deviations from three different locations of the same sample. The small standard errors indicated a small magnitude of the bias, which demonstrated that the alginate is mechanically homogeneous and can provide a simplified control.

The values of G' and G'' for the *P. aeruginosa* biofilm were 858 \pm 36 Pa and 98 \pm 12 Pa. These moduli were in the same order of magnitude as those of the synthetic biofilm sample, which indicates that the alginate sample was a reasonable surrogate of a real biofilm. Previous studies on different types of biofilms also suggested a wide range G' and G'' from rheometry tests, ranging from 10^1 - 10^3 Pa for both G' and G'' (Bol et al., 2012). The synthetic biofilm and *P. aeruginosa* biofilm in this study were within the range of reported data, with a relatively small standard deviation.

Stress relaxation tests were performed with both synthetic and *P. aeruginosa* biofilm samples (Fig. 4). The stress relaxation curve (black-square markers) demonstrates that after an initial stress response (elastic response), the viscous response recovers the stress over time when constant strain was applied on the sample. The shape of both curves indicated that both samples behaved as typical viscoelastic materials.

The fitted Maxwell model was also plotted as a green line in Fig. 4. The residual sum of squares (RSS) were compared from both samples in nonlinear least-square fitting. The RSS of synthetic biofilm was 45.4 while the RSS of homogenized *P. aeruginosa* biofilm was 152. The alginate sample had a better fit than the real biofilm. For a more accurate fitting, more elements (springs and dashpots) can be added to the Maxwell model (Peterson et al., 2013).

3.2 Comparison of experimental and simulated deformation for synthetic biofilm

In order to validate the computational biofilm model, the experimental deformation under fluid flow was determined for synthetic biofilm and homogenized *P. aeruginosa* biofilm, then compared to the model (SI V3-V4). After the rheometry tests, a portion of the same synthetic biofilm was inserted into a cylindrical mount and fixed in a flow cell for the deformation test. The position of a central cross-sectional area of synthetic biofilm was monitored in real time when a constant flow was applied. The non-deformed biofilm boundary was used as the approximate model geometry (Fig. 5) (i.e., we neglected small imperfections and fissures in the real boundary data). This approximate geometry is used to simplify the mesh generation and limit the number of elements.

With the mechanical parameters from the rheometer tests, and non-deformed synthetic biofilm geometry as the input, the simulated deformation of the synthetic biofilm in the computational model was compared to the measured deformed geometry. Based on the effluent flow rate, the averaged inflow velocity was calculated and included in the computational model. The fully developed laminar flow with a Reynolds number (Re) of $Re = 6$ was created for the inlet boundary condition. The time-dependent simulation was performed over 20 seconds, as the experimental flow was observed for the same time duration. The synthetic biofilm boundaries from simulation and experiment were superimposed with the non-deformed one (Fig. 6). The steady-state deformation in both experiment and modeling was similar, with a relative averaged error of 12.8%.

The deformation over time was also compared (Fig. 7). Three tracking points along the synthetic biofilm boundary were selected at different depths (Fig. 7a). Specifically, three parallel lines were drawn along the sample to track the horizontal displacement. The results show that the deformations in the computational model were consistent with the experimental data, with an averaged error of 24 μm (line 1), 25 μm (line 2) and 13 μm (line 3). Besides, both the model and experiment show a gradually increased displacement over the first 4-10 seconds. Then the biofilm displacement stabilized. This was due to the small velocity near the boundary compared to the velocity required for the steady-state deformation. As expected for this flow configuration, both the model and experiments show that the displacement gradually increases from base of the specimen to its tip.

The simulated velocity profile is shown in Fig. 8a and b. From the model, the x-direction velocity near synthetic biofilm geometry was around 7×10^{-5} m/s, which was around one order of magnitude smaller than the averaged velocity. The fluid flow near top and bottom boundaries travels slower than the fluid in the middle. The velocity profile of the fully developed flow was parabolic with an almost-zero velocity near the biofilm boundary. Therefore, flow with a small velocity pushed the biofilm gradually and then reached an apparent steady-state deformation. This is consistent with data from Fig. 7. Comparing the deformation at different biofilm depths, we found that the top biofilm suffered a larger displacement in the horizontal direction due to its cantilever like shape (Fig. 8). The bottom biofilm had a smaller deformation since it was anchored and closer to the stagnant zone of the velocity.

Elastic and viscous components of the deviatoric stress tensor were also plotted on the synthetic biofilm domain (Fig. 8c and d, SI V5-V6). Both elastic and viscous stresses were in the same order of magnitude, which indicated that both elasticity and viscosity contributed to biofilm deformation, according to the Oldroyd-B equation. This shows that the viscous behavior of the biofilm is not negligible, even for short time

periods.

Based on the results, it appears that the computational model can capture biofilm deformation with good accuracy. Rheometry tests in the previous section could provide a general idea on the averaged mechanical parameters for the biofilm. However, biofilm deformations are usually controlled by multiple factors, such as hydrodynamic conditions and biofilm morphologies. Thus, the study of biofilm mechanical parameters may not be enough. The simulation with hydrodynamics and biofilm morphology is necessary to predict biofilm behavior.

3.3 Comparison of experimental and simulated deformation for *P. aeruginosa* biofilm

In order to further validate the computational model, an experiment similar to the above was carried out for the *P. aeruginosa* biofilm. In this case, the Reynolds number was $Re=48$. The biofilm depth was greater than the depth of field of OCT, so only upper part was imaged.

The experimental and model-predicted deformations over time was compared for three locations on the boundary of the *P. aeruginosa* biofilm (Fig. 9). The relative average error between model-predicted displacement and experimentally measured displacement for the three points was 22.2%. The averaged error was $2.28\ \mu\text{m}$ for the tracked point on line 1, $3.05\ \mu\text{m}$ for line 2, and $1.73\ \mu\text{m}$ for line 3. The relative averaged error was larger (22%) compared to the alginate biofilm data (13%). This is expected, because the *P. aeruginosa* biofilm geometry was more complex than that of the alginate biofilm.

The steady-state displacement was in good agreement with the experiment, with consistent values among all the tracking positions. On the other hand, the simulated deformation took longer time to reach a plateau compared to the experimental data. This difference may due to the simplified geometry used in the model. The more dendritic and porous morphology of the real biofilm may introduce more water content, affecting the biofilm mechanical properties and physical behavior. Also, the simplification from irregular 3D structure to the 2D morphology could also lead to deviations. In all, it was concluded that the computational model is consistent with the experimental deformation.

3.4 Implications

Our results show that the computational model can predict the deformation of biofilms under fluid flow. Biofilms often are spatially heterogeneous in morphology and mechanical properties, which makes the prediction of their mechanical behavior more complex. Moreover, the biofilm boundary is also complex and influences the response. In our research, we studied a synthetic biofilm and a real (homogenized) biofilm. Future studies should address real biofilms with greater mechanical heterogeneity, and more complex geometries. Such studies could help clarify when the average mechanical properties are suitable for predicting deformation, and when variable properties are needed. Moreover, effects of complex boundaries should be addressed.

The PF model's ability to simulate large deformations, and its versatility with respect to the type of constitutive equations and mechanical properties, makes it useful for a wide range of problems. It also could be expanded to include biofilm growth, allowing the assessment of deformation under timescales where growth could be significant. It also could include multiple phases within the biofilm matrix, such as voids or solid precipitates, or spatially variable mechanical properties. The model would be ideal to study the effect of biofilm disruptors, which diffuse into the biofilm and weaken the EPS matrix, on biofilm removal.

A weakness of the model is that the numerical instability of Oldroyd-B constitutive equation could limit its use for higher velocity ranges and a larger relaxation time scales. However, some of these computational problems could be reduced using sharp interface and extra stabilization methods. Finally, detailed 3D simulations under complex flow regimes would require large computational recourses.

4. Conclusions

This study for the first time validates a PF computational model with the Oldroyd-B constitutive equation for biofilms, using independently determined biofilm mechanical properties. Shear rheometer results indi-

cated the mixture of alginate and bacteria cells as a reasonable surrogate for biofilm. The developed PF model captured deformations of biofilms in a real fluid environment. The results of homogenous synthetic biofilm showed a 12.8% error distance between modeling and experimental geometries after the fluid driven deformation. Homogenized real biofilm had a larger error (22.2%), possibly caused by the greater spatial heterogeneity in mechanical properties as well as complex biofilm geometry. Our study provides a promising way to capture and to predict biofilm viscoelastic behavior.

Acknowledgements

This research was partially funded by NSF GOALI #1805406, awarded to RN. ML was partially supported by the CEST/Bayer Predoctoral Research Fellowship at the University of Notre Dame. The rheology tests were performed with instruments at the Notre Dame's ND Energy Materials Characterization Facility. The computational resources to run COMSOL Multiphysics were provided by the Notre Dame Center for Research Computing (CRC). The *P. aeruginosa* strain was provided by Joshua Shrout. Cale Harnish is thanked for his help with the phase field model.

References

Alpkvist, E., & Klapper, I. (2007). Description of mechanical response including detachment using a novel particle model of biofilm/flow interaction. *Water Science and Technology* , 55 (8–9), 265–273.

Alpkvist, E., Picioreanu, C., van Loosdrecht, M. C. M., & Heyden, A. (2006). Three-dimensional biofilm model with individual cells and continuum EPS matrix. *Biotechnology and Bioengineering* , 94 (5), 961–979.

Areias, P., & Matouš, K. (2008). Finite element formulation for modeling nonlinear viscoelastic elastomers. *Computer Methods in Applied Mechanics and Engineering* , 197 (51–52), 4702–4717.

Aybar, M., Perez-Calleja, P., Li, M., Pavissich, J. P., & Nerenberg, R. (2019). Predation creates unique void layer in membrane-aerated biofilms. *Water Research* , 149 , 232–242. <https://doi.org/https://doi.org/10.1016/j.watres.2018.1>

Bai, F., He, X., Yang, X., Zhou, R., & Wang, C. (2017). Three dimensional phase-field investigation of droplet formation in microfluidic flow focusing devices with experimental validation. *International Journal of Multiphase Flow* , 93 , 130–141.

Blauert, F., Horn, H., & Wagner, M. (2015). Time-resolved biofilm deformation measurements using optical coherence tomography. *Biotechnology and Bioengineering* , 112 (9), 1893–1905.

Böl, M., Ehret, A. E., Bolea Albero, A., Hellriegel, J., & Krull, R. (2012). Recent advances in mechanical characterisation of biofilm and their significance for material modelling. *Critical Reviews in Biotechnology* , 8551 (August 2015), 1–27. <https://doi.org/10.3109/07388551.2012.679250>

Chen, A. Y., Deng, Z., Billings, A. N., Seker, U. O. S., Lu, M. Y., Citorik, R. J., ... Lu, T. K. (2014). Synthesis and patterning of tunable multiscale materials with engineered cells. *Nature Materials* , 13 (5), 515.

Craven, T. J., Rees, J. M., & Zimmerman, W. B. (2006). Stabilised finite element modelling of oldroyd-B viscoelastic flows. In *COMSOL Conference* .

Desmond, P., Best, J. P., Morgenroth, E., & Derlon, N. (2018). Linking composition of extracellular polymeric substances (EPS) to the physical structure and hydraulic resistance of membrane biofilms. *Water Research* , 132 , 211–221.

Draget, K. I., Ostgaard, K., & Smidsrod, O. (1991). Homogeneous Alginate Gels : A Technical Approach, 14 , 159–178.

Dupin, H. J., Kitanidis, P. K., & McCarty, P. L. (2001). Pore-scale modeling of biological clogging due to aggregate expansion: A material mechanics approach. *Water Resources Research* , 37 (12), 2965–2979.

Eberl, C., Thompson, R., Gianola, D., Sharpe Jr, W., & Hemker, K. (2006). Digital image correlation and tracking. *MatLabCentral, Mathworks File Exchange Server, FileID* , 12413 .

Ehret, A. E., & Bol, M. (2013). Modelling mechanical characteristics of microbial biofilms by network theory. *Journal of The Royal Society Interface* , 10 (78), 20120676.

Flemming, H.-C., & Wingender, J. (2010). The biofilm matrix. *Nature Reviews. Microbiology* , 8 (9), 623–633. <https://doi.org/10.1038/nrmicro2415>

Galy, O., Latour-Lambert, P., Zrelli, K., Ghigo, J. M., Beloin, C., & Henry, N. (2012). Mapping of bacterial biofilm local mechanics by magnetic microparticle actuation. *Biophysical Journal* ,103 (6), 1400–1408. <https://doi.org/10.1016/j.bpj.2012.07.001>

Gao, L.-T., Feng, X.-Q., & Gao, H. (2009). A phase field method for simulating morphological evolution of vesicles in electric fields. *Journal of Computational Physics* , 228 (11), 4162–4181.

Gloag, E. S., Fabbri, S., Wozniak, D. J., & Stoodley, P. (2019). Biofilm mechanics: implications in infection and survival. *Biofilm* , 100017.

Hall-Stoodley, L., Costerton, J. W., & Stoodley, P. (2004). Bacterial biofilms: from the natural environment to infectious diseases. *Nature Reviews Microbiology* , 2 (February), 95–108. <https://doi.org/10.1038/nrmicro821>

Han, G., Han, Z., Luo, A. A., & Liu, B. (2015). Three-Dimensional Phase-Field Simulation and Experimental Validation of β -Mg 17 Al 12 Phase Precipitation in Mg-Al-Based Alloys. *Metallurgical and Materials Transactions A* , 46 (2), 948–962.

Hughes, T. J. R. (2012). *The finite element method: linear static and dynamic finite element analysis* . Courier Corporation.

Jafari, M., Desmond, P., van Loosdrecht, M. C. M., Derlon, N., Morgenroth, E., & Picioreanu, C. (2018). Effect of biofilm structural deformation on hydraulic resistance during ultrafiltration: A numerical and experimental study. *Water Research* , 145 , 375–387.

Jones, W. L., Sutton, M. P., McKittrick, L., & Stewart, P. S. (2011). Chemical and antimicrobial treatments change the viscoelastic properties of bacterial biofilms. *Biofouling* , 27 (2), 207–215. <https://doi.org/10.1080/08927014.2011.5>

Kim, J. (2012). Phase-Field Models for Multi-Component Fluid Flows, 12 (3), 613–661. <https://doi.org/10.4208/cicp.301110.0>

Klapper, I., Rupp, C. J., Cargo, R., Purvedorj, B., & Stoodley, P. (2002). Viscoelastic fluid description of bacterial biofilm material properties. *Biotechnology and Bioengineering* , 80 (3), 289–296. <https://doi.org/10.1002/bit.10376>

Klapper, Isaac, & Dockery, J. (2010). Mathematical description of microbial biofilms. *SIAM Review* , 52 (2), 221–265.

Lapidou, C S, Rittmann, B. E., & Karamanos, S. A. (2005). Finite element modeling to expand the UMCCA model to describe biofilm mechanical behavior. *Water Science and Technology* , 52 (7), 161–166.

Lapidou, Chrysi S, & Rittmann, B. E. (2004). Modeling the development of biofilm density including active bacteria, inert biomass, and extracellular polymeric substances. *Water Research* ,38 (14), 3349–3361.

Liou, H.-C., Sabba, F., Packman, A. I., Wells, G., & Balogun, O. (2019). Nondestructive characterization of soft materials and biofilms by measurement of guided elastic wave propagation using optical coherence elastography. *Soft Matter* , 15 (4), 575–586.

Mokbel, D., Abels, H., & Aland, S. (2018). A phase-field model for fluid–structure interaction. *Journal of Computational Physics* ,372 , 823–840.

Nguyen, T. T., Yvonnet, J., Bornert, M., Chateau, C., Sab, K., Romani, R., & Le Roy, R. (2016). On the choice of parameters in the phase field method for simulating crack initiation with experimental validation. *International Journal of Fracture* , 197 (2), 213–226.

Paul, E., Ochoa, J. C., Pechaud, Y., Liu, Y., & Liné, A. (2012). Effect of shear stress and growth conditions on detachment and physical properties of biofilms. *Water Research* , 46 (17), 5499–5508.

Pavissich, J., Li, M., & Nerenberg, R. (2020). Spatial heterogeneity of mechanical properties of *Pseudomonas aeruginosa* biofilms, and its impacts on biofilm deformation. *Manuscript Submitted for Publication* .

Pawar, S. N., & Edgar, K. J. (2012). Biomaterials Alginate derivatization : A review of chemistry , properties and applications. *Biomaterials* , 33 (11), 3279–3305. <https://doi.org/10.1016/j.biomaterials.2012.01.007>

Peterson, B. W., van der Mei, H. C., Sjollem, J., Busscher, H. J., & Sharma, P. K. (2013). A Distinguishable Role of eDNA in the Viscoelastic Relaxation of. *MBio* , 4 (5), 1–7. <https://doi.org/10.1128/mBio.00497-13>.Invited

Pham, K. H., Ravi-Chandar, K., & Landis, C. M. (2017). Experimental validation of a phase-field model for fracture. *International Journal of Fracture* , 205 (1), 83–101.

Picioreanu, C., Blauert, F., Horn, H., & Wagner, M. (2018). Determination of mechanical properties of biofilms by modelling the deformation measured using optical coherence tomography. *Water Research* , 145 , 588–598.

Picioreanu, C., Van Loosdrecht, M. C. M., & Heijnen, J. J. (2001). Two-dimensional model of biofilm detachment caused by internal stress from liquid flow. *Biotechnology & Bioengineering* , 72 (2), 205–218.

Purevdorj, B., Costerton, J. W., & Stoodley, P. (2002). Influence of hydrodynamics and cell signaling on the structure and behavior of *Pseudomonas aeruginosa* biofilms. *Appl. Environ. Microbiol.* , 68 (9), 4457–4464.

Radu, A. I., Vrouwenvelder, J. S., Van Loosdrecht, M. C. M., & Picioreanu, C. (2010). Modeling the effect of biofilm formation on reverse osmosis performance: flux, feed channel pressure drop and solute passage. *Journal of Membrane Science* , 365 (1–2), 1–15.

Rajagopal, M. C., & Das, S. K. (2016). Analyses of drag on viscoelastic liquid infused bio-inspired patterned surfaces. *Journal of Non-Newtonian Fluid Mechanics* , 228 , 17–30.

Rubenstein, D., Yin, W., & Frame, M. D. (2015). *Biofluid mechanics: an introduction to fluid mechanics, macrocirculation, and microcirculation* . Academic Press.

Schindelin, J., Arganda-Carreras, I., Frise, E., Kaynig, V., Longair, M., Pietzsch, T., ... Schmid, B. (2012). Fiji: an open-source platform for biological-image analysis. *Nature Methods* , 9 (7), 676.

Shaheen, M., Scott, C., & Ashbolt, N. J. (2019). Long-term persistence of infectious *Legionella* with free-living amoebae in drinking water biofilms. *International Journal of Hygiene and Environmental Health* , 222 (4), 678–686.

Shaw, T., Winston, M., Rupp, C. J., Klapper, I., & Stoodley, P. (2004). Commonality of elastic relaxation times in biofilms. *Physical Review Letters* , 93 (9), 98102.

Shen, Y., Monroy, G. L., Derlon, N., Janjaroen, D., Huang, C., Morgenroth, E., ... Nguyen, T. H. (2015). Role of biofilm roughness and hydrodynamic conditions in *Legionella pneumophila* adhesion to and detachment from simulated drinking water biofilms. *Environmental Science & Technology* , 49 (7), 4274–4282.

Simoës, M., Simoës, L. C., & Vieira, M. J. (2009). Species association increases biofilm resistance to chemical and mechanical treatments. *Water Research* , 43 (1), 229–237. <https://doi.org/10.1016/j.watres.2008.10.010>

Stewart, P. S. (1993). A model of biofilm detachment. *Biotechnology and Bioengineering* , 41 (1), 111–117.

Stoodley, P., Cargo, R., Rupp, C. J., Wilson, S., & Klapper, I. (2002). Biofilm material properties as related to shear-induced deformation and detachment phenomena. *Journal of Industrial Microbiology and Biotechnology* , 29 (6), 361–367. <https://doi.org/10.1038/sj.jim.7000282>

- Stoodley, Paul, Lewandowski, Z., Boyle, J. D., & Lappin-Scott, H. M. (1999). Structural deformation of bacterial biofilms caused by short-term fluctuations in fluid shear: An in situ investigation of biofilm rheology. *Biotechnology and Bioengineering* , 65 (1), 83–92.
- Sutherland, I. W. (2001). Biofilm exopolysaccharides: A strong and sticky framework. *Microbiology* , 147 (1), 3–9. <https://doi.org/10.1099/00221287-147-1-3>
- Taherzadeh, D., Picioreanu, C., Kuttler, U., Simone, A., Wall, W. A., & Horn, H. (2010). Computational study of the drag and oscillatory movement of biofilm streamers in fast flows. *Biotechnology and Bioengineering* , 105 (3), 600–610. <https://doi.org/10.1002/bit.22551>
- Tallawi, M., Opitz, M., & Lieleg, O. (2017). Modulation of the mechanical properties of bacterial biofilms in response to environmental challenges. *Biomater. Sci.* <https://doi.org/10.1039/C6BM00832A>
- Tierra, G., Pavissich, J. P., Nerenberg, R., Xu, Z., & Alber, M. S. (2015). Multicomponent model of deformation and detachment of a biofilm under fluid flow. *Journal of The Royal Society Interface* ,12 (106), 20150045.
- Towler, B. W., Cunningham, A., Stoodley, P., & McKittrick, L. (2007). A model of fluid–biofilm interaction using a Burger material law. *Biotechnology and Bioengineering* , 96 (2), 259–271.
- Towler, B. W., Rupp, C. J., Cunningham, A. L. B., & Stoodley, P. (2003). Viscoelastic properties of a mixed culture biofilm from rheometer creep analysis. *Biofouling* , 19 (5), 279–285.
- Wen, Y. H., Wang, Y., Bendersky, L. A., & Chen, L.-Q. (2000). Microstructural evolution during the $\alpha 2$ - $\alpha 2 + o$ transformation in Ti–Al–Nb alloys: phase-field simulation and experimental validation. *Acta Materialia* , 48 (16), 4125–4135.
- Wéry, N., Bru-Adan, V., Minervini, C., Delgènes, J.-P., Garrelly, L., & Godon, J.-J. (2008). Dynamics of Legionella spp. and bacterial populations during the proliferation of L. pneumophila in a cooling tower facility. *Appl. Environ. Microbiol.* , 74 (10), 3030–3037.
- Xavier, J. B., Picioreanu, C., Abdul Rani, S., van Loosdrecht, M. C. M., & Stewart, P. S. (2005). Biofilm-control strategies based on enzymic disruption of the extracellular polymeric substance matrix - A modelling study. *Microbiology* , 151 (12), 3817–3832. <https://doi.org/10.1099/mic.0.28165-0>
- Xavier, J. de B., Picioreanu, C., & van Loosdrecht, M. C. M. (2005). A general description of detachment for multidimensional modelling of biofilms. *Biotechnology and Bioengineering* , 91 (6), 651–669.
- Yue, P., Zhou, C., Feng, J. J., & Hu, H. H. (2006). Phase-field simulations of interfacial dynamics in viscoelastic fluids using finite elements with adaptive meshing, 219 , 47–67. <https://doi.org/10.1016/j.jcp.2006.03.016>
- Zhang, T., Cogan, N. G., & Wang, Q. (2008a). Phase field models for biofilms. I. Theory and one-dimensional simulations. *SIAM Journal on Applied Mathematics* , 69 (3), 641–669.
- Zhang, T., Cogan, N., & Wang, Q. (2008b). Phase field models for biofilms. II. 2-D numerical simulations of biofilm-flow interaction. *Commun. Comput. Phys* , 4 (1), 72–101.
- Zhang, Y., Wang, H., & Tang, T. (2010). Simulating two-phase viscoelastic flows using moving finite element methods. *Communications in Computational Physics* , 7 (2), 333.
- Zhao, J., Shen, Y., Haapasalo, M., Wang, Z., & Wang, Q. (2016). A 3D numerical study of antimicrobial persistence in heterogeneous multi-species biofilms. *Journal of Theoretical Biology* ,392 , 83–98.
- Zheng, X., & Karniadakis, G. E. (2016). A phase-field/ALE method for simulating fluid–structure interactions in two-phase flow. *Computer Methods in Applied Mechanics and Engineering* ,309 , 19–40.

Table 1. Parameters used in the model

| Name | Value | Units | Description | Source |
|-------------|----------------------|-------------------|--|---------------------------|
| u_1 | 6×10^{-4} | m/s | Average flow velocity for synthetic biofilm test | Experiment |
| | 4.8×10^{-3} | | Average flow velocity for homogenized biofilm test | |
| χ | 1×10^{-9} | m[?]/s/kg | Mobility parameter | from Zhang et al. (2008b) |
| ϑ | 1×10^{-2} | N/m | Surface tension coefficient | from Koza et al. (2009) |
| ρ_s | 1000 | kg/m ³ | Solvent density | Value at 20°C |
| μ_s | 0.001 | Pa[?]/s | Viscosity of solvent | Value at 20°C |
| ρ_b | 1000 | kg/m ³ | Biofilm density | Assumed |
| μ_b | 30494 | Pa[?]/s | Viscosity of synthetic biofilm | Experiment |
| | 78705 | | Viscosity of homogenized biofilm | |
| G_b | 69736 | Pa | Shear modulus of synthetic biofilm | Experiment |
| | 46851 | | Shear modulus of homogenized biofilm | |

Figure Legends

Fig. 1. Schematic indicating the coordinate system and modeling dimensions in the flow cell. The schematic is not to scale.

Fig. 2. Schematic of experimental set up, including biofilm flow cell and OCT unit. The flow was driven by gravity.

Fig. 3. Averaged viscoelastic moduli for synthetic biofilm and homogenized *P. aeruginosa* biofilm. The error bars show standard deviations from 3 replicates.

Fig. 4. Rheometer data and fitted Maxwell model for (a) synthetic biofilm, and (b) homogenized biofilm. The synthetic biofilm was tested under a constant strain of 0.01% and the homogenized biofilm was under 0.1% of strain. The black square markers indicate the averaged measured shear stress over time. The error bars indicate one standard deviation, based on the 10 replicates. The green line shows the fitted Maxwell model.

Fig. 5. Biofilm geometries in the experiment and model. (a) Cross-sectional OCT image of synthetic biofilm; (b) modeling geometry based on the OCT image.

Fig. 6. The comparison of synthetic biofilm boundaries. Flow was from left to right. Green line: biofilm contour at $t=0$ (in experiment and computational model); black line: biofilm contour at $t=20$ s (in experiment); black dashed line: biofilm contour at $t=20$ s (in computational model). Unrelated data were filtered out.

Fig. 7. (a) Locations of measurement (lines 1-3) for DIC analysis. (b)-(d) Experimental and modeling displacement of synthetic biofilm along lines 1-3.

Fig. 8. Simulated velocity \mathbf{u} and stress distribution for synthetic biofilm at $t=2$ s. (a) Velocity field of solvent domain (colored surface and black arrows); (b) velocity field of synthetic biofilm domain (colored arrows); (c) the magnitude of viscous stress tensor $\|\tau\|$ on synthetic biofilm domain; (d) the magnitude of elastic components of the deviatoric stress tensor $\|\sigma_e\|$ on synthetic biofilm domain.

Fig. 9. (a) Locations of measurement (lines 1-3) for DIC analysis. (b)-(d) Experimental and modeling displacement of *P. aeruginosa* biofilm along lines 1-3.

Hosted file

Figures_BB.pdf available at <https://authorea.com/users/312181/articles/442784-predicting-biofilm-deformation-with-a-viscoelastic-phase-field-model-modeling-and-experimental-studies>

Figure 1

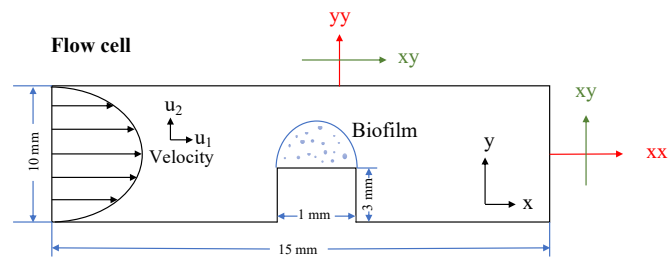


Fig. 1. Schematic indicating the coordinate system and modeling dimensions in the flow cell. The schematic is not to scale.